Comparative time-resolved photoemission from the Cu(100) and Cu(111) surfaces

Marcelo J. Ambrosio and Uwe Thumm

J. R. Macdonald Laboratory, Department of Physics, Kansas State University, Manhattan, Kansas 66506, USA

Motivated by the striking dependence of the valence electronic structure of transition metal surfaces on their crystallographic orientation, and by emerging experiments on laser-assisted extended ultraviolet (XUV) photoemission from solid surfaces, we calculate photoemission spectra from Cu(100) and Cu(111) surfaces as a function of the photoelectron final kinetic energy and the delay between the ionizing attosecond XUV pulse train and assisting infrared (IR) laser pulse. Our numerical simulations predict distinct differences in delay-dependent photoelectron energy distributions and photoemission time delays for Cu(100) and Cu(111) surfaces. These differences can be scrutinized experimentally with existing technology in a suggested *in situ* comparative RABBITT (reconstruction of attosecond beating by interference of two-photon transitions) configuration by placing the two surfaces on a sliding platform while keeping all optical components and pathlengths fixed. Our calculations also show that the inclusion of the Fresnel-reflected incident IR pulse at the metal-vacuum interface modifies photoelectron spectra and photoemission time delays in a characteristic way that reveals the degree of spatial location of the initial electronic states.

I. INTRODUCTION

Photoelectron emission is one of the most fundamental processes in nature. It occurs upon the incidence of electromagnetic radiation with sufficiently short wavelength on matter, proceeds through the coupling of the incident radiation with electrons, and results in the transfer of photonic energy to one or more electrons. These photoelectrons leave the target and carry information about the photoemission dynamics and the electronic properties of the target material. The analysis of their detectable energy and momentum distribution has been one of the most prolific methods for determining the electronic structure of gaseous atoms and molecules, solids, and solid surfaces [1]. For more than a century, attempts to better understand measured photoelectron spectra required and promoted the development of quantum mechanics. Photoelectron spectroscopy based on light sources that do not allow time resolution of the interatomic electronic dynamics have been routinely employed for many decades and remain a preferred tool for imaging electronic structure in the energy domain. Energy-domain spectra are sensitive to the target's ultrafast internal electronic dynamics during the photoemission process but do not resolve the time-dependent electronic dynamics during the photoelectron-release process.

Starting in the year 2001, continued progress in ultrafast laser technology enabled the generation of attosecond pulse trains (APTs) [2] and isolated attosecond pulses (IAPs) [3–5] that allow for investigations of the electronic dynamics in atoms, molecules, and condensed matter systems. These time-resolved investigations complement energy-domain spectroscopies and involve two types of experimental setups: streaked photoelectron emission and reconstruction of attosecond beating by interference of two-photon transitions (RABBITT). In streaking experiments, photoemission is induced by an IAP, typically with a broad frequency spectrum in the extreme ultraviolet (XUV) range, and photoelectrons are emitted into the electric field of a delayed infrared (IR) pulse [6–9]. By recording photoelectron energy spectra as a function of the delay between the IAP and IR pulse for XUV pulse lengths that are smaller than the optical period of the streaking IR

pulse, streaked photoemission spectra can be obtained. These spectra reveal temporal information through delay-dependent photoelectron energy shifts that oscillate with the frequency of the IR-laser pulse, reducing the measurement of ultrashort time intervals (of the order of 10 attoseconds, 1 atomic unit of time = 1 a.u. = 24 as = 24 $\times 10^{-18}$ s) to observable energy shifts.

The RABBITT technique [2,10–12] relies on photoelectron emission by an APT in the electric field of a delayed IR-laser pulse. In comparison to streaking spectroscopy, it has two main advantages. First, APTs are easier to generate in the laboratory than IAPs and second, it requires intensities of the assisting IR pulse that are typically an order of magnitude smaller than the IR intensities in streaking experiments, thereby minimizing transient distortions of the target by the measurement while providing spectra of comparable temporal and spectral resolution [13]. APTs are assembled as superpositions of higher harmonics (HHs) of the IR-pulse central frequency. In RABBITT spectra, two-path interferences lead to spectral sidebands (SBs) in which the photoelectron yield oscillates as a function of the XUV-IR delay with twice the frequency of the IR pulse. At IR intensities employed in typical RABBITT experiments and assumed in this work, each path involves ionization by a single HH photon and either absorption or stimulated emission of an IR photon. Both pathways result in the same final photoelectron energy. A SB of order $2n$ (SB$2n$) is the result of the interference of ionization by a HH harmonic photon of order $2n - 1$ and absorption of an IR photon and a second pathway, given by the ionization by an HH photon of order $2n + 1$ and emission of an IR photon (Fig. 1). SBs in RABBITT spectra are energetically separated by twice the IR-photon energy. A given SB (SB$2n$) is energetically centered a single IR-photon energy below the energy of photoelectrons that are emitted after the absorption of a single HH photon of order $2n + 1$. The SB lies a single IR-photon energy above photoelectrons that result from single-photon electron emission by a HH harmonic photon of order $2n - 1$. Temporal information, such as relative photoemission time delays, is retrieved from SB-yield oscillations in RABBITT spectra. The
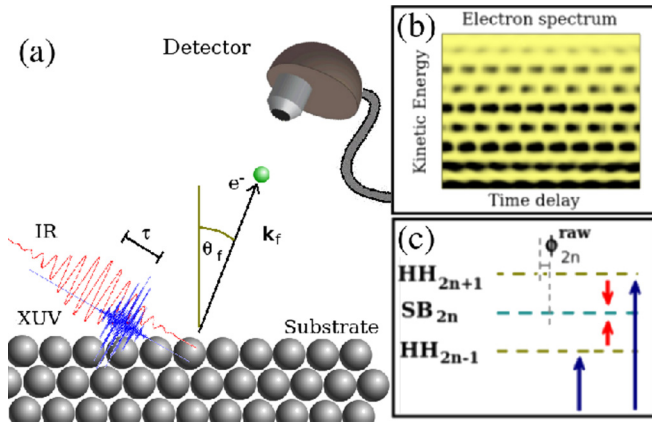
FIG. 1. Schematic of the RABBITT experimental setup. (a) An XUV attosecond pulse train and delayed IR pulse with linear polarization in the reflection plane are incident on a surface. The attosecond pulse train emits electrons that are detected with momentum $\mathbf{k_f}$. (b) A typical RABBITT spectrum, revealing phaseshifts between photoelectron sideband-yield oscillations. (c) Sideband-yield oscillations are the result of a two-path XUV-IR two-photon interference process.

detection of ultrashort time intervals from RABBITT spectra is thus based on the measurement of delay-dependent yield oscillations.

The HH constituents of APTs are produced by coherent HH generation (HHG) with XUV frequencies that are equal to odd multiples of the primary IR-pulse frequency and are characterized by their amplitudes and relative phases. The temporal profile of APTs is typically not well determined, as the relative HH phases are not known to the best of our knowledge. Since the temporal information is encoded in the relative phases, RABBITT SB-yield oscillations depend on the HH phases. It is therefore desirable to seek methods for eliminating the unknown HH phases. The elimination of the HH phases is possible by illuminating different targets with the same optical set up, i.e., identical APTs and IR pulses, followed by the investigation of phase differences between RABBITT SB traces from different targets for the same HH orders. Such phase differences have been recently studied for photoemission from atomic targets [14] as well as solid surfaces [12,15] and will be further investigated in this work.

While streaked photoemission spectra have been recorded and modeled in many experiments [3,7,16] and theoretical investigations [16,17] for gaseous atomic targets, comparatively few time-resolved experimental [8,18,19] and theoretical [20,21] studies were carried out for solid targets [22]. This is attributable to both, experimental challenges in preparing clean and atomically flat solid surfaces and the more complicated nature of photoemission from complex targets. In comparison to isolated gaseous atoms, photoemission from solids involves a complex electronic band structure [15,23], elastic and inelastic scattering of released photoelectrons inside the solid, including the excitation of surface and bulk plasmons [24–26], as well as dielectric screening [27] and reflection [13] of the assisting IR-laser field at the solid surface. While streaked photoemission from surfaces has been investigated for almost a decade, RABBITT spectra have

only been recorded and analyzed very recently from solid surfaces [12,15], a notable precursor being SB studies [28,29], where the photoelectron spectra generated by a long XUV pulse and a time-delayed IR pulse were recorded. Locher *et al.* [12] analyzed RABBITT photoelectron spectra from Au(111) and Ag(111) surfaces, eliminating unknown HH phases by subtracting RABBITT phases measured with the same experimental setup (yet different optical path lengths) from gaseous argon. Tao *et al.* [15] performed RABBITT experiments on Ni(111) surfaces with emphasis on the propagation of released photoelectrons in the substrate. By comparing photoelectron excitation into unoccupied excited states of the Ni(111) band structure and into free-electron-like states as a function of the photoelectron emission angle, the authors found significant differences in photoemission lifetimes. They concluded that details of the substrate band structure matter for the propagation of excited photoelectrons, even at photoelectron kinetic energies of the order of 30 eV.

While the comparative RABBITT method applied by Locher *et al.* [12] relates RABBITT spectra recorded with the same optical system on surfaces to a reference atomic target positioned at a different location, we suggest to *directly* compare spectra from two surfaces that are placed at the *same* location. This can be realized by installing the two surfaces on a sliding platform and eliminates the need for determining the optical path-lengths difference between the two target locations and associated SB phase shifts in RABBITT spectra (cf. Supplemental Material in Ref. [12]), while keeping the advantage of allowing the elimination of the unknown HH phases. The different surfaces can be either made of different materials or different crystallographic orientations of the same material. For our theoretical study in this paper, we consider Cu(100) and Cu(111) surfaces, which have been widely investigated in energy-domain-spectroscopy and particle-scattering studies [30–38]. A similar type of comparative RABBITT study has been applied to two different atomic shells of gaseous argon targets [11]. We note that a comparison between the Cu(100) and Cu(111) surfaces was carried out previously, within a different area of atomic and surface physics by Chakraborty *et al.* [37], who investigated electron detachment from H^- during grazing incidence collisions with Cu(100) and Cu(111) surfaces. In their study, different hydrogen-anions-neutralization rates were traced to the different valence electronic structures of the two surfaces; in particular, to the transient population of the Cu(111) surface state (SS) that impedes electronic decay into the solid in comparison with more rapid H^- neutralization near Cu(100) surfaces.

We organized this paper as follows. In Sec. II we describe our numerical model. Next, in Sec. III, we present and discuss numerical results for raw RABBITT spectra, difference RABBITT spectra, and photoemission phases and time delays. In the comparative discussion of spectra and time delays, we focus on effects that are due to differences in the electronic structures of Cu(100) and Cu(111) surfaces and assess the importance of including the reflected IR field in theoretical calculations. Section IV contains our summary and conclusions. In two appendices, we present details of the theoretical description of SB structures in RABBITT spectra (Appendix A) and the effect of the surface-reflected IR pulse on photoemission from the Cu(111) SS (Appendix B). We use

atomic units ($\hbar = e = m_e = 1$) throughout this work, unless specified otherwise. When given in units of electronvolts, we relate electron energies to the ionization threshold at $\varepsilon = 0$ eV, unless stated otherwise.

II. THEORY

A. Initial states

In the single-active-electron approximation, assuming translational invariance in the surface plane and using Cartesian coordinates, valence electronic states

$$\Psi_{\mathbf{k}_i}^i(\mathbf{r},t) = \frac{e^{-i\varepsilon_{\mathbf{k}_i}t}}{2\pi}e^{i\mathbf{k}_{i\parallel}\cdot\mathbf{r}_\parallel}\psi_i(z) \qquad (1)$$

of the substrate factorize as the product of a plane wave with momentum $\mathbf{k}_{i\parallel}$ in the surface and a one-dimensional wave function $\psi_i(z)$ for the electronic motion in direction perpendicular to the surface. Translational invariance in the surface plane was assumed previously in the modeling of photoemission in direction perpendicular to a surface [23,39]. In our coordinate system, the surface is coincident with the x-y plane and the z axis is normal to the surface.

We model the valence electronic structure of Cu(100) and Cu(111) surfaces using effective "Chulkov" potentials. These potentials are given as parameterized analytical functions of the electronic z coordinate, and the open parameters are adjusted to the results of density-function calculations and experiments [36]. The Cu(100) potential reflects the known smaller interplanar distance along the z axis, $a_s = 3.415$, compared to $a_s = 3.94$ for Cu(111) [36], has a larger oscillation amplitude below the surface plane, and a shallower well at the surface (Fig. 2). We calculated the wave functions $\psi_i(z)$ as eigenstates of the Hamiltonian consisting of the electronic kinetic energy operator, including the full electron mass of 1 a.u., and the Chulkov potentials for the (100) or (111) surfaces, representing the substrate as a 900 a.u. thick slab on a 20 000 point numerical grid. The symmetrical slab is bounded by Chulkov potentials on either side. Our numerical results show that Cu(100) and Cu(111) surfaces exhibit very different valence electronic structures [36,37]. The Chulkov potentials yield a single energy band of stationary states for each substrate. For the given parametrization of the Cu(100) and Cu(111) Chulkov potentials, and in good agreement with measured photoelectron spectra (cf. Ref. [36] and references therein), we find that the Cu(111) valence spectrum exhibits a 5.23 eV wide projected L-band gap, a long-lived SS that is energetically located inside the band gap, and a series of image states of which the lowest lies in the band gap, while higher image states are degenerate with the conduction band. For the Cu(100) surface, our calculation reproduces the X-band gap, the bottom of which lies 2.33 eV above the bottom of the Cu(111) band gap and extends into the continuum beyond the ionization threshold. In comparison, the Cu(111) band gap is confined to energies below the ionization threshold. In contrast to the Cu(111) surface, the Cu(100) surface has a broad SS that is degenerate with the valence band, and all Cu(100) image states are degenerate with the X-band gap.

Next, within the spectrum of Cu(100) and Cu(111) electronic states generated by the respective parameterized potentials, we select the range of *occupied* initial states in
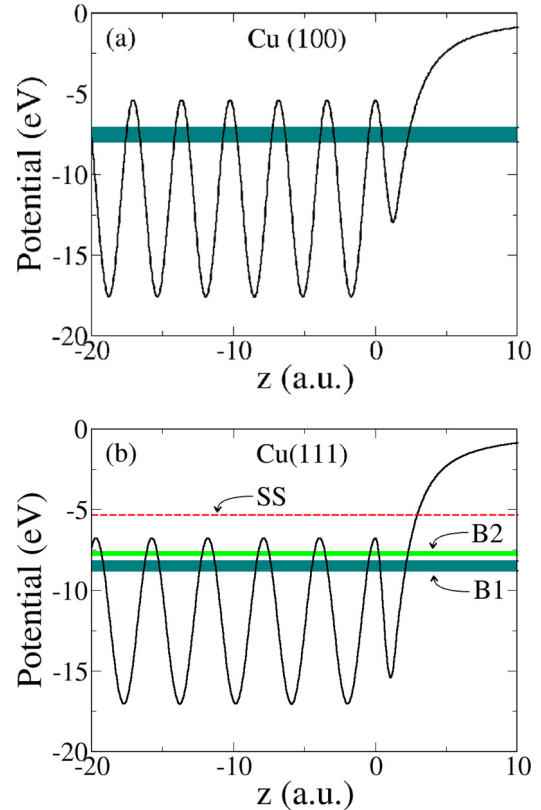
FIG. 2. Effective potentials [36] and spectral range of the occupied states adapted from Ref. [38] for (a) Cu(100) and (b) Cu(111). The occupied part of the valence bands are indicated by colored (gray) stripes. The Cu(111) surface state (SS) is shown as the horizontal dashed red line in (b).

compliance with recent angle–resolved photoelectron spectra measured for normal emission by Roth *et al.* [38] (Fig. 2). For photon energies between 25 and 35 eV, corresponding to the range of photon energies in a recent RABBITT experiment on Au and Ag surfaces [12], Fig. 1 in Ref. [38] suggests the Cu(100) surface to have occupied initial valence states with energies between -3.4 and -2.5 eV below the Cu(100) Fermi level at $E_F^{(100)} = -4.62$ eV [36], while occupied valence states of the Cu(111) surface appear in two intervals that we refer to as "B1" and "B2 bands." These Cu(111) bands extend from -3.8 to -3.2 eV (B1 band) and from -2.9 to -2.7 eV (B2 band) relative to the Fermi energy $E_F^{(111)} = -4.94$ eV [36]. In addition to initial states in the B1 and B2 band, we include the occupied Cu(111) SS at a binding energy of -5.33 eV (0.39 eV below $E_F^{(111)}$). Within the finite numerical grid we use to diagonalize the Chulkov Hamiltonian, the occupied part of the valence band of Cu(100) is represented by a discretized continuum of 19 states, while the B1 and B2 bands of Cu(111) are numerically modeled with 14 and 6 states, respectively, using the parameterization from Ref. [36]. The Cu(111) occupied valence band is thus represented by 20 states, plus the SS ψ_{SS}. In contrast to bulk states of the Cu valence bands, the Cu(111) SS is localized at the surface, and its probability density extends to significantly larger distances into the vacuum half-space (Fig. 3). This difference in spatial
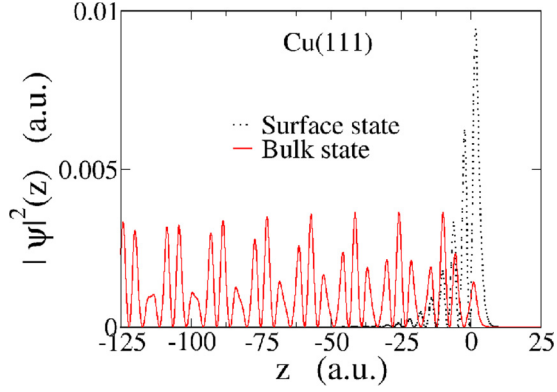
FIG. 3. Probability densities of the Cu(111) bulk state with binding energy -7.78 eV and the Cu(111) surface state.

localization has a pronounced effect on RABBITT specta, as we will discuss in Sec. III.

As we will investigate in Sec. III, initial-state momentum distributions influence the photoelectron spectra in characteristic ways. For this reason, we show in Fig. 4 the envelopes of the net momentum distributions,

$$A(p_z) = \max_{i \in \text{occ.}} |\tilde{\psi}_i(p_z)|, \qquad (2)$$

of the occupied parts of the Cu(100) valence band, the B1 and B2 bands of Cu(111), as well as the momentum distribution
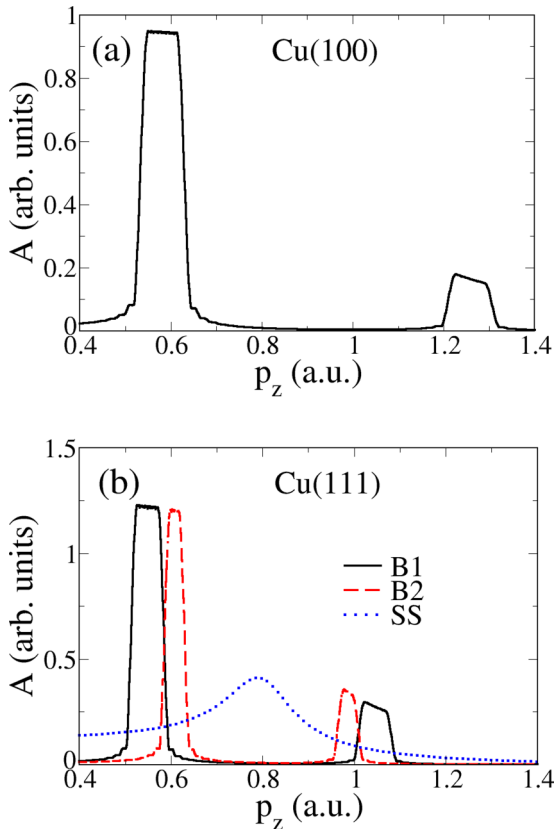
FIG. 4. Envelope $A(p_z)$ of the momentum distributions of the occupied valence bands of (a) Cu(100) and (b) Cu(111) and the Cu(111) surface state (SS) [cf. Eq. (2)].

$\tilde{\psi}_{SS}(p_z)$ of the Cu(111) SS. The momentum distributions are obtained by Fourier transformation of the initial wave functions $\psi_i(z)$. By plotting the envelope $A(p_z)$ for valence-band states, we focus on the overall momentum content of a given band. According to Eq. (2), $A(p_z)$ is calculated for every given momentum p_z as the largest amplitude of all occupied states in a given band. Due to the reflection symmetry of the 900 a.u. thick Cu slab, all initial states are either symmetrical or antisymmetrical with regard to the slab center, such that $A(p_z) = A(-p_z)$. While the probability distribution of the Cu(111) SS is concentrated at the surface, resulting in a comparatively broad momentum distribution, the momentum distributions of the three considered bands of bulk states are each concentrated at two distinct values of $|p_z|$.

Physically, the lower momenta, centered near $|p_z| = 0.58$ for Cu(100), 0.57 for the B1 band, and 0.60 for the B2 band of Cu(111), correspond to the valence electronic motion in the classically allowed regions, i.e., in the valleys of the Chulkov potential (Fig. 2). The higher momenta in these distributions, centered near $|p_z| = 1.25$ for Cu(100), 1.05 for the B1 band, and 0.95 for the B2 band of Cu(111), are associated with the behavior of the wavefunctions in the classically forbidden regions between local minima of the bulk potential. The lower (higher) momentum peak of the B2 band in Fig. 4 appears at slightly larger (smaller) momenta $|p_z|$ than the lower (higher) peak of the B1 band. For comparison, representing the Cu valence bands in jellium approximation [40] with potential-well depth U_0, the corresponding states have peaks only at a single momentum $|p_z| = |\sqrt{2m(\varepsilon_i + U_0)}|$, corresponding to the lower momentum peaks in Fig. 4.

B. Fresnel-reflected IR-laser pulse

For p polarization (linear polarization of the IR-electric field in the reflection plane), the photoelectron is exposed to the total IR electric field

$$\mathbf{E}_{\text{IR}}(\mathbf{r},t) = \mathcal{E}_{\text{IR}}(t)[\mathbf{E}_{\text{ext}}(z)\mu(z) + \mathbf{E}_{\text{int}}(z)\mu(-z)], \qquad (3)$$

which can be written as the product of the time-dependent factor

$$\mathcal{E}_{\text{IR}}(t) = \mathcal{E}_{\text{IR}}^{(0)} e^{-2\ln(2)(t/\sigma_{\text{IR}})^2} e^{i(\omega_{\text{IR}}t + \phi_{\text{CEP}})} \qquad (4)$$

and the superposition of the external and internal Fresnel fields

$$\mathbf{E}_{\text{ext}}(z) = \hat{\mathbf{z}}[e^{i(-\frac{\omega_{\text{IR}}}{c}z\cos\alpha)} + R e^{i(\frac{\omega_{\text{IR}}}{c}z\cos\alpha)}]\sin\alpha \qquad (5)$$

and

$$\mathbf{E}_{\text{int}}(z) = \hat{\mathbf{z}}T e^{i(-\frac{\omega_{\text{IR}}}{c}z\cos\beta)}\sin\beta, \qquad (6)$$

respectively [41]. σ_{IR} and ϕ_{CEP} designate the electric field's temporal full width at half maximum (FWHM) and carrier-envelope phase. In Eqs. (5) and (6), we neglect the component of the Fresnel-reflected IR field in direction parallel to the surface. This component is much smaller then the normal component due to the cancellation of the tangential field components of the incident and reflected wave, while the surface-normal components superimpose constructively. The surface component of the transmitted field is about an order of magnitude smaller than the outside electric field and negligible at grazing incidence of the IR pulse.

The complex transmission and reflection coefficients in (5) and (6) are given by Fresnel's equations [41],

$$R = \frac{\varepsilon'(\omega_{IR})\tan\beta - \varepsilon(\omega_{IR})\tan\alpha}{\varepsilon'(\omega_{IR})\tan\beta + \varepsilon(\omega_{IR})\tan\alpha}, \qquad (7a)$$

$$T = \frac{2n'(\omega_{IR})\varepsilon(\omega_{IR})}{n(\omega_{IR})\varepsilon'(\omega_{IR})}\frac{\varepsilon'(\omega_{IR})\tan\beta}{\varepsilon'(\omega_{IR})\tan\beta + \varepsilon(\omega_{IR})\tan\alpha}. \qquad (7b)$$

The angle of incidence α and the refraction angle $\beta = \sin^{-1}(n\sin\alpha/n')$ are measured relative to the surface normal. In our application, $n(\omega_{IR}) = 1$ is the refraction index on the vacuum side of the surface. As the refraction index n' is complex, the electric field inside the substrate decays exponentially, constituting an evanescent wave. Equations (5) and (6) are macroscopic in nature and correct at large distances from the surface. At the atomic length scale, however, they present an abrupt change from the outside to the inside electric field at the surface, since (within macroscopic electromagnetic theory) the normal component of the electric field is not continuous across an interface between media with different refraction indices. In order to smoothly connect internal and external Fresnel fields across the top two atomic layers, we therefore introduce the matching function

$$\mu(z) = \frac{1}{2}\left[\tanh\left(\frac{2z}{\delta_{IR}}\right) + 1\right] \qquad (8)$$

and continuously connect $\mathbf{E}_{ext}$ and $\mathbf{E}_{int}$, where δ_{IR} is the IR skin depth. We approximate δ_{IR} by the interlayer spacings a_s of the Cu(100) and Cu(111) surfaces. The assumption of small IR skin depths of the order of 5 a.u. matches the skin-depth deduced from streaked photoemission spectra of Mg-covered W surfaces by Neppl et al. [8].

We describe the Cu-surfaces' response to the incident IR pulse within the Drude-Lorentz model with the dielectric function

$$\varepsilon'(\omega) = \varepsilon^f(\omega) + \varepsilon^b(\omega), \qquad (9a)$$

$$\varepsilon^f(\omega) = 1 - \frac{f_0\omega_p}{\omega(\omega - i\Gamma_0)}, \qquad (9b)$$

$$\varepsilon^b(\omega) = \sum_{j=1}^{N_{osc}} \frac{f_j\omega_p^2}{(\omega_j^2 - \omega^2) + i\omega\Gamma_j}. \qquad (9c)$$

The free-electron term $\varepsilon^f(\omega)$ is a result of the Drude model, and the interband term $\varepsilon^b(\omega)$ is modeled by Lorentz oscillators with frequencies ω_j originally introduced to describe the dielectric properties of insulators [42]. The parameters ω_p, N_{osc}, f_j, and Γ_j are the plasma frequency, oscillator strengths, and inverse lifetimes. These parameters have been tabulated for various materials [43]. For the IR frequencies near $\omega_{IR} = 1.5$ eV used in this work, the Drude-Lorentz model provides a sufficiently accurate description of the dielectric function [43] and agrees with optical experiments [44]. At $\omega_{IR} = 1.5$ eV, it yields the dielectric constant $\varepsilon'(\omega_{IR}) = (-27.50 + 2.51i)$ and corresponding index of refraction $n(\omega_{IR}) = \sqrt{\varepsilon'(\omega_{IR})} = (0.24 + 5.25i)$, taking into account that copper is not ferromagnetic.

For our numerical applications in Sec. III, we use IR-field parameters comparable to parameters of the RAB-

BITT experiment by Locher et al. [12]. Our p-polarized IR pulse is characterized by $\alpha = 75°$, a peak intensity of 10^{11} W/cm^2, $\sigma_{IR} = 6$ fs, a central wavelength of 827 nm, and $\phi_{CEP} = 0$. For the Drude-Lorentz dielectric response of Cu, the amplitude of the surface-parallel component of the external IR field is five times smaller than the normal component, justifying our neglect of the parallel component of $\mathbf{E}_{IR}(\mathbf{r},t)$ in Eqs. (5) and (6). While we represent $\mathbf{E}_{IR}$ in this subsection as a complex-valued function, in order to conveniently keep track of the phases of $\mathbf{E}_{ext}(z)$ and $\mathbf{E}_{int}(z)$, we note that only the real part of $\mathbf{E}_{IR}$, $\Re(\mathbf{E}_{IR})$, is relevant for our calculation of the photoemission amplitude spectra below.

C. Final state

We represent the final continuum state of the photoelectron as a Volkov wave function

$$\Psi_{\mathbf{k}_f}^f(\mathbf{r},t,\tau) = \frac{f_{\varepsilon_f,\theta_f}(z)}{(2\pi)^{3/2}} e^{i[\mathbf{k}_f + \mathbf{A}_{IR}(\mathbf{r},t_d)]\cdot\mathbf{r}}$$
$$\times e^{i\phi_{\mathbf{k}_f}(\mathbf{r},t_d) - i\varepsilon_{\mathbf{k}_f}t} \qquad (10)$$

that is modified by the factor

$$f_{\varepsilon_f,\theta_f}(z) = \Theta(z) + e^{z/[2\lambda(\varepsilon_f)\cos(\theta_f)]}\Theta(-z), \qquad (11)$$

where $\Theta(z)$ is the Heaviside step function, in order to account for an exponential damping of the photoelectron probability density in terms of the energy-dependent mean free path $\lambda(\varepsilon_f)$ and the emission angle θ_f [21]. The mean free path accounts for collisions of a released photoelectron inside the solid that may prevent its emission. Due to elastic and inelastic collisions, an electron, even if given enough energy by the APT to overcome the potential increase at the surface, is thus very unlikely to be emitted if it has to traverse a distance comparable to or larger than $2\lambda(\varepsilon_f)$ in the substrate before reaching the surface. For our numerical applications in Sec. III, we employ energy-dependent inelastic mean free paths calculated by Tanuma et al. [45] based on experimental optical data and consider emission in normal direction ($\theta_f = 0$). The parameter τ is the adjustable time delay between the IR pulse and the XUV APT: positive τ values mean that the IR pulse arrives after the XUV APT, and we define $t_d = t - \tau$.

IR-pulse intensities in typical RABBITT experiments are low enough so that the ponderomotive energy of the photoelectron can be safely neglected. The "Volkov phase" in (10) is then given by [21,23]

$$\phi_{\mathbf{k}_f}(\mathbf{r},t) = \int_t^\infty dt' \mathbf{k}_f \cdot \mathbf{A}_{IR}(\mathbf{r},t') \qquad (12)$$

in terms of the IR-pulse vector potential

$$\mathbf{A}_{IR}(\mathbf{r},t) = \int_t^\infty \Re[\mathbf{E}_{IR}(\mathbf{r},t')]dt'. \qquad (13)$$

As discussed in the previous subsection, $\mathbf{A}_{IR}$ includes the incident IR pulse and its reflection at the surface.

D. Attosecond pulse train

The electric field of the XUV APT is generated by the superposition of odd HHs of ω_{IR} with amplitudes $\mathbf{E}_{0,2n+1}$,

widths σ_{2n+1} (FWHM), and central frequencies $\omega_{2n+1} = (2n+1)\omega_{IR}$,

$$\mathbf{E}_{XUV}(t) = \sum_n \mathbf{E}_{0,2n+1} e^{-2\ln(2)[(\omega-\omega_{2n+1})/\sigma_{2n+1}]^2}$$
$$\times \cos\left(\omega_{2n+1}t + \phi_{2n+1}^{HH}\right). \tag{14}$$

The phases ϕ_{2n+1}^{HH} are typically unknown and very difficult to determine both experimentally [14] and theoretically [46–48]. However, it is possible to extract phase information from RABBITT spectra without knowledge of the HH phases by calculating phase differences from two spectra [12]. We will follow up on this idea in Sec. III such that the HH phases become irrelevant with regard to the phase-difference analysis of our calculated RABBITT spectra. The HH phases, however, do matter for individual RABBITT spectra, and in order to calculate and discuss them, we (arbitrarily) set $\phi_{2n+1}^{HH} = 0$ for all contributing harmonics in (14).

As for the IR pulse, we select the APT parameters in compliance with the experiment performed by Locher *et al.* [12], including odd HHs from $2n+1 = 15$ to 21, each component with a spectral width σ_{2n+1} of 1 eV. As mentioned above, the absorption of a photon from the APT with energy ω_{2n+1} and emission of an IR photon leads to the same final photoelectron kinetic energy, $\varepsilon_{\mathbf{k}_f} = 2n\omega_{IR} + \varepsilon_{\mathbf{k}_i}$, as the absorption of a photon from the APT with energy ω_{2n-1} and absorption of an IR photon. This results in interference oscillations of the photoelectron yield at photoelectron energies at and near $2n\omega_{IR} + \varepsilon_{\mathbf{k}_i}$, i.e., to delay-dependent intensity oscillations of the SBs SB2n in the RABBITT spectrum (here: SB16, SB18, and SB20). We do not take into account the attenuation of the APT inside the Cu substrate in (14) because it is negligible over the photoelectron mean free paths in our calculation of the photoemission spectrum.

E. Photoemission amplitude

The transition matrix element for electron emission due to the absorption of a single photon from the APT is [21]

$$T_{\mathbf{k}_f,\mathbf{k}_i}(\tau) = \frac{1}{i}\int_{-\infty}^{\infty} dt\left\langle\Psi_{\mathbf{k}_f}^f(\mathbf{r},t,\tau)\big|zE_{XUV}(t)\big|\Psi_{\mathbf{k}_i}^i(\mathbf{r},t)\right\rangle$$
$$= \frac{1}{i}\int_{-\infty}^{\infty} dt\, D_{\mathbf{k}_i,\mathbf{k}_f} E_{XUV}(t)e^{i(\varepsilon_i-\varepsilon_f)t}, \tag{15}$$

with the dipole element

$$D_{\mathbf{k}_i,\mathbf{k}_f} = \frac{\delta(\mathbf{k}_{f\parallel}-\mathbf{k}_{i\parallel})}{(2\pi)^{3/2}}\int dz\, e^{-i[k_{fz}+A_{IR,z}(z,t_d)]z}$$
$$\times e^{-i\phi_{\mathbf{k}_f}(z,t_d)} f_{\varepsilon_f,\theta_f}(z)z\psi_i(z). \tag{16}$$

$A_{IR,z}(z,t)$ is the normal component of the vector potential (13). It can be considered as independent of the surface coordinates x and y, consistent with the assumptions already justified for $\mathbf{E}_{IR}(\mathbf{r},t)$. Note that the Volkov phase depends on the normal coordinate z, due to the spatial nonuniformity of the net IR-electric field (3). This is in contrast to atomic photoionization, where a typically z-independent IR vector potential imposes a spatially uniform momentum shift at time t_d [19].

According to (15), the probability of an electron to be subject to single-XUV-photon emission or a two-photon
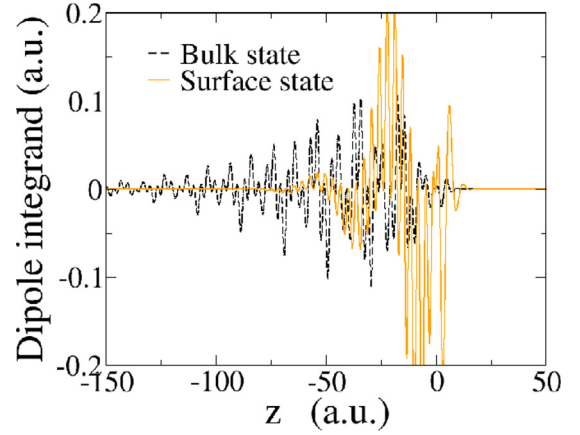
FIG. 5. Real part of the integrand of the dipole element (16) for photoemission from a Cu(111) bulk state with binding energy -7.78 eV and the Cu(111) surface state.

transition involving an XUV and an IR photon depends on the time- and position-dependent coupling of its initial state ψ_i to its final modified Volkov state. The probability for an XUV-IR two-photon transition therefore strongly depends on the IR skin depth of the substrate, which is represented by the matching function $\mu(z)$. This is demonstrated in the discussion of our numerical results in Sec. III below.

The dipole approximation in (16) is valid because the damping function $f_{\varepsilon_f,\theta_f}(z)$ causes the main contribution to $D_{\mathbf{k}_i,\mathbf{k}_f}$ to come from a small interval extending from the surface to a few lattice spacings into the substrate. The length of this interval is smaller than the wavelength (about 40 nm) of the highest harmonic ($n = 21$) included in the APT (14).

The strong spatial localization of the Cu(111) SS in combination with the small IR skin depth and XUV transparency (on the scale of the electron mean free path) significantly enhances the relative influence of the IR field on SS photoemission by an XUV APT in comparison with photoemission from bulk states. This is confirmed in our numerical studies discussed in Sec. III B below, and can also be inferred from the integrand in (16) (Fig. 5).

The photoemission probability per unit surface area for a given final momentum $\mathbf{k}_f$ and time delay τ is obtained by the incoherent inclusion of all occupied initial states [49],

$$P(\mathbf{k}_f,\tau) = \int d\mathbf{k}_i|T_{\mathbf{k}_f,\mathbf{k}_i}(\tau)|^2. \tag{17}$$

It is instructive to investigate the contribution of individual initial-state momentum components to the photoelectron yield. For this purpose, we express the initial state in terms of its momentum-space wave function,

$$\psi_i(z) = (2\pi)^{-3/2}\int dp\,\tilde{\psi}_i(p)e^{ipz}, \tag{18}$$

and rewrite the dipole matrix element as

$$D_{\mathbf{k}_i,\mathbf{k}_f} = \frac{\delta(\mathbf{k}_{f\parallel}-\mathbf{k}_{i\parallel})}{(2\pi)^3}\int dp\,\tilde{\psi}_i(p)$$
$$\times \int_{-\infty}^{\infty} dz\, z f_{\varepsilon_f,\theta_f}(z)e^{-i\phi_{\mathbf{k}_f}(z,t_d)}e^{i(p-k_{fz}-A_{IR,z}(z,t_d))z}.$$
$$\tag{19}$$

Written in this form, the oscillating phase factor $e^{i(p-k_{fz}-A_{IR,z}(z,t_d))}$ suggests both, momentum matching,

$$p = k_{fz} + A_{IR,z}(z,t_d), \qquad (20)$$

and significant initial momentum-space probability density $|\tilde{\psi}_i(p)|^2$ as necessary requirements for efficient photoemission into final states with final normal momentum component k_{fz}. This agrees with the simple interpretation of the photoelectron receiving at time t_d a local momentum transfer $A_{IR,z}(z,t_d)$ from the IR-pulse electric field. Initial states with a broad momentum distribution are thus expected to contribute to photoelectron spectra more uniformly over a broader photo-electron energy range than spatially delocalized initial states, which are characterized by a comparatively narrow momentum distribution [25]. As an example, we consider the top part of the Cu(100) momentum distribution for Cu(100) in Fig. 4(a), which includes momenta from approximately 1.2 to 1.3 a.u. According to Eq. (20) this distribution contributes to more significant emission of photoelectrons in the 20 to 23 eV energy range. Similarly, for Cu(111) the momentum components between 0.9 and 1.1 a.u. [Fig. 4(b)] lead to enhanced emission from the Cu(111) B1 and B2 bands of photoelectrons with final kinetic energy between 12 and 16 eV. In contrast, over a large energy range, the SS momentum spectrum does not have an abrupt cutoff, but changes smoothly as the momentum grows, leading to a more uniform energy dependence of the emission probabilities.

III. NUMERICAL RESULTS AND DISCUSSIONS

Throughout this manuscript, we refer to delay-dependent photoelectron spectra obtained according to Eq. (17) as "raw" RABBITT spectra. For bulk states the XUV+IR two-photon yield is small in comparison to the yield for single-photon emission in just the APT, due to the strong attenuation of the IR pulse inside the bulk and high XUV transparency. In order to better display the for RABBITT spectra characteristic two-pathway two-photon interference effects, we calculate differences between raw RABBITT and single-XUV-photon ionization yields. The latter we obtain from the same code by setting the IR-pulse intensity equal to zero. We refer to these difference spectra as "XUV-subtracted" spectra.

We will refer to "raw RABBITT phases" as the phases of yield oscillations in raw RABBITT spectra relative to the phase of the IR-pulse; or, more precisely, relative to the maximal overlap between the incident IR pulse and APT, defining $\tau = 0$. The same raw phases are retrieved from raw and XUV-subtracted spectra (the XUV subtration does not affect the phases). We designate differences between raw RABBITT phases for the same SB order of two RABBITT spectra as "relative RABBITT phases." In contrast to raw phases, relative phases are independent of the HH phases $\phi_{2n+1}^{(HH)}$. Similarly, time delays corresponding to raw and relative phases will be referred to as "raw" and "relative time delays," respectively.

A. Initial-state dependence of Cu(100/111) RABBITT spectra

Figure 6 shows XUV-subtracted RABBITT spectra for Cu(100) and Cu(111) surfaces. In particular, for photoemission from bulk valence states, the subtraction of the single-XUV-
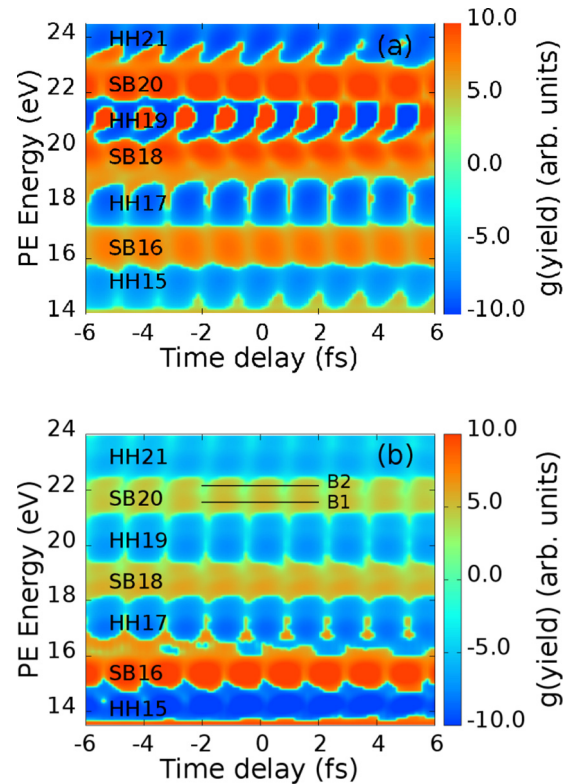
FIG. 6. XUV-subtracted RABBITT spectra [photoelectron-yield difference on the bi-symmetric logarithmic scale (21)] for photoemission from the valence bands of (a) Cu(100) and (b) Cu(111). The horizontal black lines in (b) indicate contributions from the B1 and B2 bands.

photon ionization yield is necessary for clearly revealing SB intensity oscillations. The electronic probability density of bulk states is distributed over the entire substrate, while the IR pulse is strongly attenuated within the first two atomic layers. On the other hand, the XUV APT propagates through the substrate essentially unimpeded [50]. Since XUV-subtracted RABBITT spectra have positive and negative yield differences y that extend over many orders of magnitude, we show the spectra on a bi-symmetric logarithmic scale [51]

$$g(y) = \text{sgn}(y)\log(1 + |y/C|). \qquad (21)$$

The XUV-subtracted spectra in Fig. 6 are displayed setting the scale factor $C = 10^{-5}$.

The XUV-subtracted spectrum for Cu(100) in Fig. 6(a) shows pronounced yield-difference oscillations at photoelectron energies from 20 to 23 eV, corresponding to the HH spectral components 19 and 21 of the APT, while for the Cu(111) spectrum [Fig. 6(b)] the yield difference is largest for HHs 15 and 17. In both spectra, the yields for different photoelectron energies are consistent with the initial states' momentum distributions in Fig. 4. Dominantly contributing high momenta lie in the intervals between 1.2 and 1.3 a.u. in Fig. 4(a) and 0.9 and 1.1 a.u. in Fig. 4(b), respectively, for the Cu(100) and Cu(111) surfaces. In terms of final kinetic energies, these momentum intervals translate to strong yields between 19 and 23 eV for Cu(100), and between 11 and 16 eV for Cu(111).
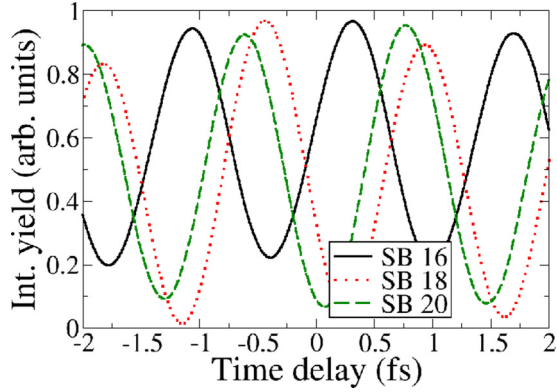
FIG. 7. Integrated raw RABBITT photoelectron yields for sidebands 16 to 20 for photoemission from a Cu(100) surface (independently normalized).

FIG. 8. RABBITT phases for valence-band photoemission from Cu(100) and Cu(111) surfaces, relative to the RABBITT phase for photoemission from the surface state of Cu(111).

Negative difference yields in the XUV-subtracted spectrum can result from destructive interference of the XUV absorption and the single-IR-photon transition [cf. Appendix A]. Negative differences occur primarily on the HH traces due to the loss of emission probability to two-photon transitions. However, as indicated in the HH19 trace in Fig. 6(a), differences with respect to pure XUV photoemission can also be positive. This is not surprising, since the dipole matrix element, including the Fresnel-reflected IR pulse (19), entails a widened momentum matching (20), coupling initial and final states more intricately and differently than without the Fresnel-reflected pulse.

Closer inspection of Fig. 6(b) allows the distinction of contributions to the yields in SBs 18 and 20 and HH bands 17 and 19 from the B1 and B2 valence bands of Cu(111). Photoelectron yields from the B2 band (lower band limit −8.8 eV, upper band limit −8.2 eV) appear at slightly higher energies than for emission from the B1 band (lower band limit −7.8 eV, upper band limit −7.6 eV) (cf. Fig. 2). At lower photoelectron energies (HH15 and SB16), contributions from the B1 and B2 band cannot be distinguished, as the higher SB-yield contributions from the B1 band eclipse those from the B2 band. This is easily understood from the momentum-matching condition (20) and the bands' momentum compositions. Following Fig. 4, we can estimate for emission from the B1 band a large electron yield for final energies between 13.6 and 16.5 eV, while for the B2 band photoelectron energies extend from 12.3 to 14.3 eV, which is below SB16.

From the XUV-subtracted RABBITT spectrum we estimate the energetic width of a given SB due to emission from a given energy band in the substrate. Integration over the SB width in the raw and XUV-subtracted spectra leads to "integrated raw SB yields" [12] and "integrated XUV-subtracted SB yields." We selected energy intervals for the yield integration of 1 eV for Cu(100) and 0.6 eV for Cu(111), centered at the corresponding SB, in order to include most of the SB yield, while avoiding overlapping contributions from neighboring SBs. As an example, Fig. 7 shows integrated yields for SBs 16 to 20 for photoemission from a Cu(100) surface.

Based on integrated XUV-subtracted SB yields, we determine raw and relative RABBITT phases and time delays. The RABBITT phases for photoemission from the Cu(100) valence band and the B1 and B2 bands of Cu(111) are shown
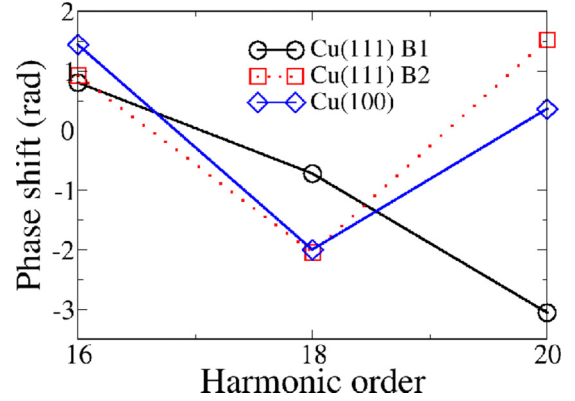
Fig. 8 relative to the raw RABBITT phases for photoemission from the SS of Cu(111). These relative phases dependent sensitively on the SB order and the initial electronic states. Our SB-yield-phase changes with the HH order are similar in magnitude to those measured for Au(111) and Ag(111) surfaces by Locher *et al.* [12]. However, in contrast to our study, the theoretical model in Ref. [12] does not predict phase oscillations with respect to the harmonic order. We intend to discuss photoemission from Ag(111) and Au(111) in a separate publication.

Relative time delays for valence-band photoemission into SBs 16 to 20 are listed in Table I. They are referenced relative to the raw time delays for photoemission from the SS of Cu(111) and exhibit oscillations in the SB order. In accord with our findings for Cu surfaces, measured time-delay variations of the order of 100 as over four SBs for emission along the surface normal were very recently reported for Ni(111) surfaces by Tao *et al.* [15].

B. Effect of Fresnel reflection

1. Emission from the Cu(111) surface state

The broad momentum spectrum of the SS tends to level differences in electron yields at different HH orders. Since the SS probability density decays quickly towards the inside of the solid, its broad momentum spectrum causes the SS to efficiently couple to final states over a comparatively

TABLE I. Relative RABBITT time delays (RTDs) for photoemission from the valence bands of Cu(100) and Cu(111), relative to emission from the SS of Cu(111), for sideband orders 16 to 20. Final photoelectron energies are given in units of eV, inelastic mean free paths (MFP, according to Ref. [45]) in a.u., and relative time delays in as.

SB	Cu(100)			Cu(111) B1			Cu(111) B2		
	$\varepsilon_{\mathbf{k}_f}$	MFP	RTD	$\varepsilon_{\mathbf{k}_f}$	MFP	RTD	$\varepsilon_{\mathbf{k}_f}$	MFP	RTD
16	16.6	17.20	318	15.6	18.15	177	16.4	17.35	204
18	19.6	15.03	−442	18.6	15.76	−160	19.4	15.16	−452
20	22.6	13.20	79	21.6	14.04	−675	22.4	13.28	336
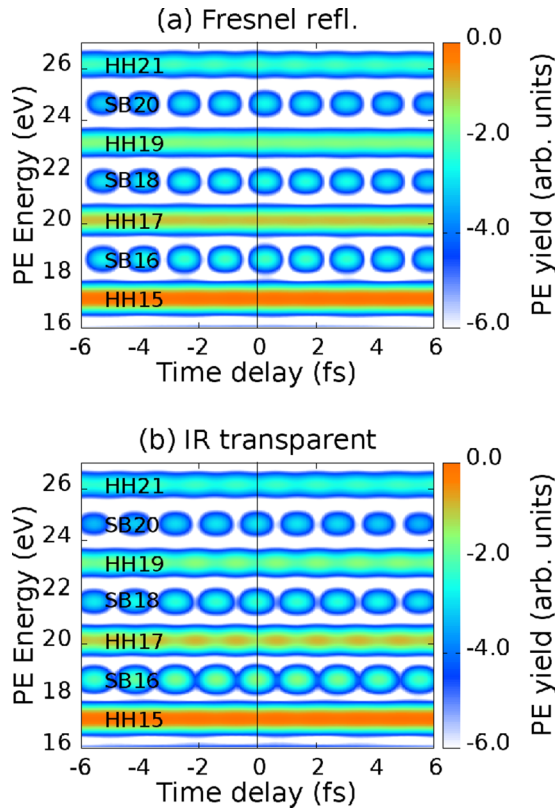
FIG. 9. Raw RABBITT spectra (independently normalized) for photoemission from the surface state of Cu(111). (a) Including Fresnel reflection of the incident IR pulse. (b) Assuming IR-transparency of the substrate. The vertical line at $\tau = 0$ facilitates the identification of phase shifts between the SB yield oscillation in (a) and (b).

FIG. 10. Raw RABBITT phases for different assumptions regarding the reflection and transmission of the incident IR pulse. Green dashed line with diamonds: Fresnel reflection. Blue dashed line with triangles: the Cu surface is assumed transparent (no reflection). Solid black line with circles: perfect reflection with continuous electric-field matching according to Eq. (8).

large photoelectron energy range [cf. Fig. 4(b) and Sec. II E above]. At the same time, extending about 20 a.u. into the vacuum, the SS is significantly more susceptible to the incident and reflected IR electric fields than bulk valence states. Accordingly, our RABBITT spectra for photoemission from the SS have noticeable electron yields for all HH orders ($2n + 1 = 15, \ldots, 21$) included in our calculations (Fig. 9). Therefore, as expected due to the surface-localization of the initial SS, the spectra in Figs. 9(a) and 9(b) are similar, but clearly not identical. The spectrum in Fig. 9(b) is calculated assuming IR-transparency of the substrate ($\varepsilon'(\omega_{IR}) = 1$). The comparison of the spectra in Fig. 9 reveals phase shifts for the SB structures at equal HH order. In addition, the ratio of SB versus HH yield in Fig. 9(a) is slightly smaller than in Fig. 9(b). Including the Fresnel-reflected wave, the IR field is enhanced outside and strongly damped inside the substrate, as compared to our results for an IR-transparent substrate. This makes XUV-IR two-photon emission in Fig. 9(a) more likely to occur on the vacuum side of the surface than in Fig. 9(b).

Figure 10 compares raw RABBITT phases for different assumptions regarding the reflection and transmission of the incident IR pulse at the surface. Phases extracted from the spectrum in Fig. 9(a) are shown as the green dashed line with diamond markers. Phases obtained under the assumption of an IR-transparent substrate, corresponding to the spectrum in Fig. 9(b) are given by triangles connected by blue dash-

dotted lines. "Perfect reflectivity" corresponds to the limit $\varepsilon'(\omega_{IR}) \to \infty$ in which the reflection and transmission coefficient in (7a) and (7b) become 1 and 0, respectively. We modeled a smooth perfect reflector, continuously extrapolating electric fields of the incident and reflected IR pulse using the matching function $\mu(z)$ (7b) in Eq. (8). The corresponding raw phases are plotted as black circles, connected by solid lines. For emission from the SS, the raw RABBITT phases for perfect reflection [$\varepsilon'(\omega_{IR}) \to \infty$] and perfect transmission [$\varepsilon'(\omega_{IR}) = 1$] are almost uniformly smaller by 1.2 rad than for the Fresnel-reflected IR wave, based on the Drude-Lorentz complex dielectric function (9). For both, perfect IR-transparency and perfect IR-transmission, where no Fresnel phase is introduced, the SS states only show small raw RABBITT phases. This, together with the fact that the phases are affected in a predictable way by the IR pulse (cf. Appendix B), makes the SS a useful reference for comparative RABBITT studies. This is relevant for the envisioned sliding-platform comparative measurement, which would eliminate the unknown HH phases $\phi_{2n+1}^{(HH)}$, but introduces the SS phases in exchange.

The real and imaginary normal components $\hat{\mathbf{z}} \cdot [\mathbf{E}_{out}(z)\mu(z) + \mathbf{E}_{in}(z)\mu(-z)]$ of the three electric fields $\mathbf{E}_{IR}$ distinguished in Fig. 10 are depicted in Fig. 11 relative to the amplitude of the incident IR pulse, for an incidence of angle $\alpha = 75°$.

2. Emission from the valence bands

Raw RABBITT spectra for emission from the valence band of Cu(100), calculated for both, a Fresnel-reflected IR pulse and assuming IR-transparency of the substrate without reflection, are shown in Fig. 12. Upon Fresnel reflection of the incident IR pulse, the net IR electric-field amplitude decays within a few surface layers inside the substrate. This leads to comparatively very small SB yields and dominant single-XUV-photon yields, without interference-generated yield oscillations [Fig. 12(a)]. The difference between spectra calculated for Fresnel-reflected IR pulses and assuming IR-transparency is further enhanced by the probability density
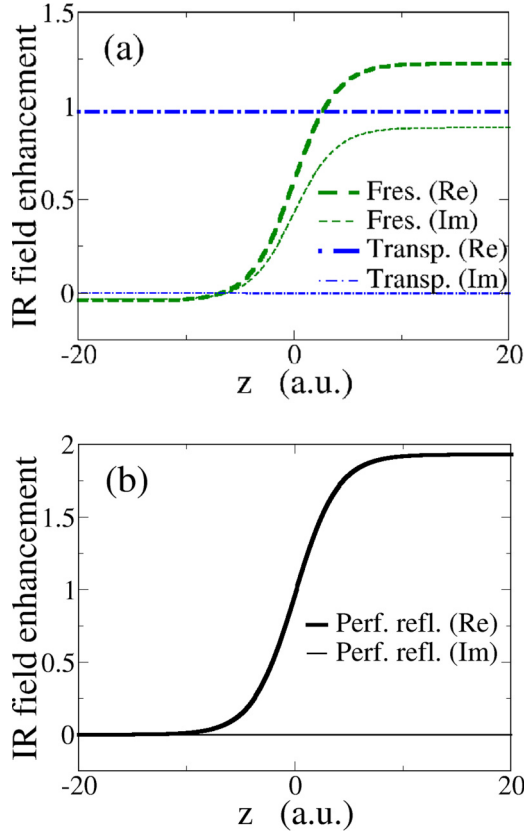
FIG. 11. Complex-valued total IR-electric-field amplitude relative to the incident IR-field amplitude. Thick lines show real, thin lines imaginary parts. (a) Green dashed line: including Fresnel reflection; Blue dash-dotted line: IR-transparent Cu surface. (b) Solid black line: perfect reflection with smeared out electric-field matching according to Eq. (8).

of bulk valence states being confined to the substrate and decaying rapidly outside the surface where higher IR-electric-field amplitudes prevail.

The almost uniform shift of the raw phases of all SBs for emission from the SS due to the inclusion of the Fresnel-reflected IR pulse (Fig. 10) is absent for photoemission from bulk valence-band states, as depicted in Fig. 13. This can be traced back to the z-dependent contributions to the dipole element (16) in Fig. 5. Due to the comparatively large extension of the SS probability density on the vacuum side of the surface, the yield for SS emission is less sensitive to the addition of the Fresnel-reflected wave than the yield for emission from bulk states, as the comparison of Figs. 9 and 12 demonstrates. The bulk states' extremely small SB and largely dominant HH amplitudes in Figs. 12(a) and 12(c) can also be understood analytically from the argument in the Bessel function in Eq. (A9) of Appendix A. As the electric-field amplitude of the Fresnel-reflected IR pulse quickly decreases inside the substrate, the argument and value of the Bessel function become small ($J_m(x) \propto x^m$). The Bessel function J_{j_2} in Eq. (A9) determines the magnitude of the SB yields relative to the neighboring HH structures. Thus the SB yields become smaller than they would be if the IR field penetrated the substrate without attenuation. This explains us showing

XUV-subtracted spectra in order to better visualize the SB oscillations in Fig. 6.

Summarizing the comparison of the spectra and phases in Figs. 9 and 12, we note that the inclusion of the surface-reflected IR pulse affects raw RABBITT spectra for emission from the SS and bulk states in completely different ways. While for emission from the SS the RABBITT spectrum changes only slightly upon inclusion of the Fresnel-reflected IR pulse (Fig. 9), for emission from bulk states inclusion of the Fresnel-reflected wave suppresses XUV-IR two-photon transitions in comparison to HH emission (Fig. 12).

We next investigate the influence of the reflected IR pulse and relative RABBITT phases for emission from the valence bands of Cu(100) and Cu(111) surfaces. In Fig. 14(a) we use the raw RABBITT phase for emission from the Cu(111) SS as a reference, in Fig. 14(b) the raw RABBITT phase for emission from the B1 valence band of Cu(111), and in Fig. 14(c) the Cu(111) B2 raw phase. Figure 14 shows that the Fresnel reflected IR-pulse cannot be neglected. It also illustrates that the choice of a reference state strongly influences RABBITT SB phases.

As the integrand of the dipole matrix element (16) in Fig. 5 reveals, for emission from bulk states, contributions to the photoemission yield are assembled from many atomic layers inside the substrate, in contrast to emission from the SS, as discussed before. Spectra for assumed IR transparency of the substrate and Fresnel reflection are therefore expected to be characterized by different raw RABBITT phases, as shown in Fig. 14. For the same reason, relative RABBITT phases that are referenced to the SS and to bulk valence states respond differently to the IR-electric field amplitude distribution near the surface and in the substrate, as the comparison of Figs. 14(a)–14(c) demonstrates. Therefore, to provide accurate relative RABBITT phases, the surface-reflected IR pulse needs to be accounted for. While this is readily expected when referencing bulk to SS emission [Fig. 14(a)], it is also true for relative RABBITT phases that reference bulk emission to bulk emission from a different band [Figs. 14(b) and 14(c)].

IV. SUMMARY

We numerically modeled RABBITT spectra for photoemission from Cu surfaces with crystallographic orientations (100) and (111) and analyzed photoelectron yields, RABBITT SB oscillations, and SB phase shifts in terms of (i) the localization character of the initial photoelectron states, (ii) their momentum distributions, (iii) depth-dependent contributions to the dipole matrix element and photoemission yield, and (iv) the electric-field amplitude distribution of the assisting IR field near the surface and inside the substrate. We represented the initial state of the photoelectrons based on an effective potential that yields the main characteristics of the valence electronic structure of both surfaces and adjusted the band limits of occupied initial states to recently obtained (X)UV photoelectron spectra in Ref. [38].

We find the localization character of the initial states to have a significant influence on RABBITT spectra. For photoemission from bulk states, XUV-subtracted spectra are more descriptive than raw spectra, since for bulk states, single-XUV-photon emission dominates the yield and obscures
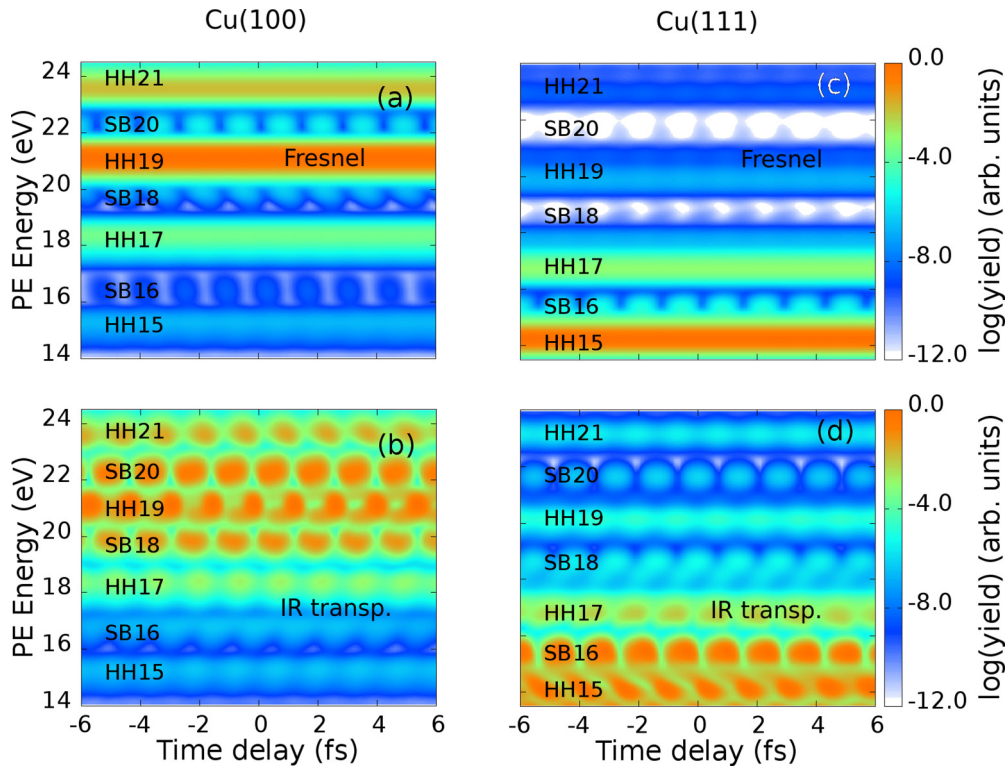
FIG. 12. Raw RABBITT spectra (independently normalized) for photoemission from bulk valence states. (a) and (b) Cu(100); (c) and (d) Cu(111). The Fresnel-reflected IR pulse is included in (a) and (c); IR-transparency is assumed in (b) and (d).

XUV-plus-IR two-photon SB emission. By analyzing raw and difference RABBITT spectra and related raw as well as relative SB phase shifts for different assumed electric-field-amplitude distributions, we demonstrate the need for including the surface-reflection of the *p*-polarized incident IR pulse. We included the reflected IR pulse based on the dielectric properties of the substrate and scrutinized its relevance for emission from the SS of Cu(111) and bulk valence states.

Discussing relative SB RABBITT phases referenced to either the SS or bulk conduction-band states, we suggest photoemission from the SS of Cu(111) as an ideal reference for the phase of SB oscillations. APTs available in the laboratory are currently not well characterizable and, in particular, the phases of their constituent HHs are typically unknown. In order to eliminate the undetermined HH phases, we therefore suggest an *in situ* RABBITT setup in which Cu(100) and Cu(111) RABBITT spectra are measured in comparison. In such an experiment, both surfaces are illuminated by the APT and IR pulse in exactly the same way, without introducing path-lengths differences, by placing the surfaces on a sliding platform. A sliding platform eliminates undetermined phase shifts that would result from the illumination of the surfaces at different locations. The comparison of SB oscillations for two surfaces, ideally in difference spectra, then allows the extraction of relative RABBITT SB phases, without prior knowledge of the HH phases of the APT.
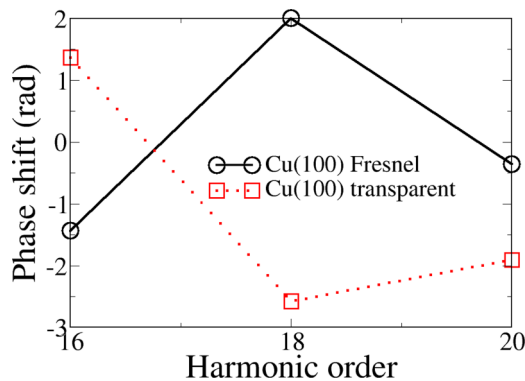
FIG. 13. Raw RABBITT phases for photoemission from the Cu(100) valence band, assuming either Fresnel reflection of the incident IR pulse or IR transparency of the substrate.

APPENDIX A: MATHEMATICAL ANATOMY OF THE SIDEBAND STRUCTURE

For the following analytical study, we assume that the IR-pulse temporal envelope $h_{\mathrm{env}}(t_d) = \mathcal{E}_{\mathrm{IR}}^{(0)} e^{-2\ln(2)\left(\frac{t_d}{\sigma_{\mathrm{IR}}}\right)^2}$ varies slowly in time and rewrite the net IR electric field (3), its corresponding vector potential, and the Volkov phase
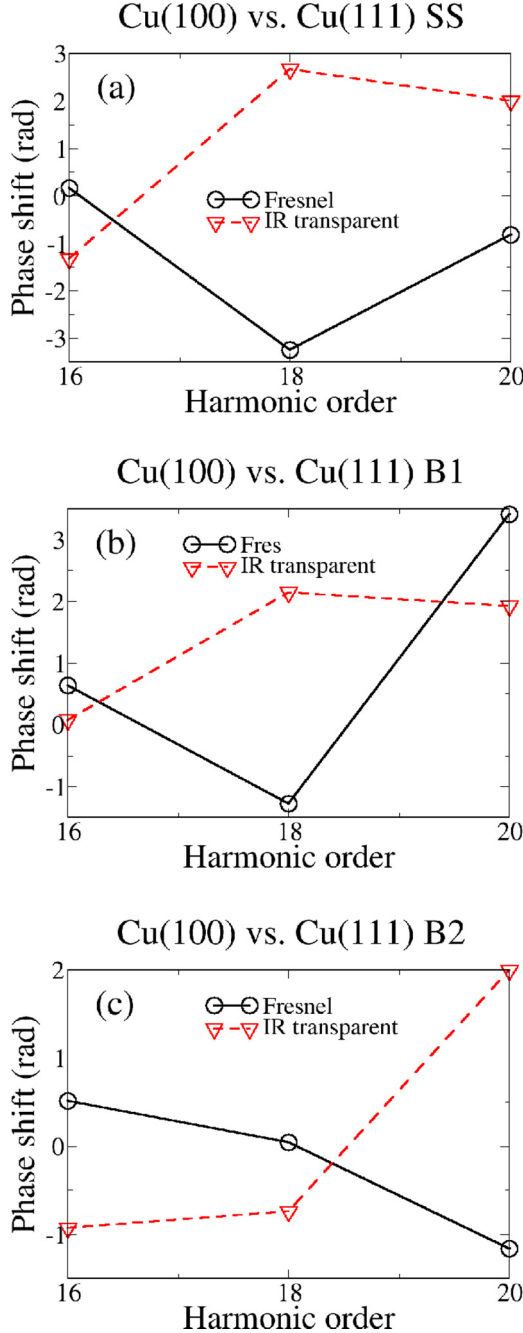
FIG. 14. Relative RABBITT phases for emission from the valence band of Cu(100), referenced against the (a) Cu(111) surface state, (b) B1 valence band of Cu(111), and (c) B2 valence band of Cu(111). Black circles connected by solid black lines show results including Fresnel reflection of the IR pulse. Red triangles interpolated with dashed red lines show calculations assuming IR transparency of the substrate.

as

$$\mathbf{E}_{IR}(\mathbf{r}, t_d) = \hat{\mathbf{z}} E_z(z) h_{env}(t_d) e^{i \, \omega_{IR} t_d}, \tag{A1}$$

$$\mathbf{A}_{IR}(\mathbf{r}, t_d) = -\hat{\mathbf{z}} E_z(z) \frac{h_{env}(t_d)}{i \, \omega_{IR}} e^{i \, \omega_{IR} t_d}, \tag{A2}$$

$$\phi_{\mathbf{k}_f}(\mathbf{r}, t_d) = \mathbf{k}_f \cdot \hat{\mathbf{z}} E_z(z) \frac{h_{env}(t_d)}{\omega_{IR}^2} e^{i \, \omega_{IR} t_d}, \tag{A3}$$

with the definition of the z-dependent part of the net IR electric field

$$E_z(z) = \hat{\mathbf{z}} \cdot [\mathbf{E}_{ext}(z)\mu(z) + \mathbf{E}_{int}(z)\mu(-z)], \tag{A4}$$

which, as a complex-valued function, can be expressed in terms of its absolute value and phase,

$$E_z(z) = |E_z(z)|[\cos(\phi_E(z)) + i \sin(\phi_E(z))]. \tag{A5}$$

For the physically relevant real part, we have

$$\Re[E_z(z)h_{env}(t_d)e^{i \, \omega_{IR} t_d}] = |E_z(z)|h_{env}(t_d)\cos(\omega_{IR}t_d + \phi_E(z)), \tag{A6}$$

recalling that Fresnel phase $\phi_E(z)$ corresponds to the phase of the total field, and not only the Fresnel-reflected pulse.

Fourier decomposition of the real part of the net IR electric field yields

$$\Re[E_z(z)h_{env}(t_d)e^{i \, \omega_{IR} t_d}]$$
$$= \int d\omega' \widetilde{E}(\omega', z) \cos(\omega' t_d + \phi_E(z) + \chi_{\omega'}), \tag{A7}$$

with amplitude $\widetilde{E}(\omega', z)$ and a phase $\chi_{\omega'}$, which vanishes for $\omega' = \omega_{IR}$. We formally approximate the above integral by a finite sum over a discrete set of frequencies ω_{j_1},

$$\int d\omega' \widetilde{E}(\omega', z) \cos(\omega' t_d + \phi_E(z) + \chi_{\omega'})$$
$$\approx \sum_{j_1} q_{j_1} \widetilde{E}(\omega_{j_1}, z) \cos\left(\omega_{j_1} t_d + \frac{\phi_E(z) + \chi_{\omega_{j_1}}}{\omega_{j_1}}\right), \tag{A8}$$

with quadrature weights q_{j_1} given by the selected numerical-integration method (Gaus-Legendre, Simpson, trapezoids, etc.) [52].

The dependence of the Volkov phase on the Fresnel phase is obvious in the phase factor

$$e^{i\phi_{\mathbf{k}_f}(\mathbf{r},t_d)} \approx \prod_{j_1} \left[\sum_{j_2} J_{j_2}\left(\frac{q_{j_1}\mathbf{k}_f \cdot \hat{\mathbf{z}}}{\omega_{IR}^2} \widetilde{E}(\omega_{j_1}, z)\right) \right.$$
$$\left. \times i^{j_2} e^{ij_2\omega_{j_1}(\omega_{j_1}t_d + \phi_E(z) + \chi_{\omega_{j_1}})} \right] \tag{A9}$$

of the final Volkov state (10). We note that our numerical simulations presented in the main body of this manuscript do not involve the assumption of a slowly-varying envelope made in this appendix.

APPENDIX B: INFLUENCE OF THE FRESNEL PHASE ON THE SS RABBITT PHASES

For the SS let us assume that the dipole-matrix-element integration in Eq. (16) vanishes inside the substrate, such that only the vacuum-side IR field contributes to IR emission or absorption. Furthermore, we assume the limiting macroscopic case, for which the matching function $\mu(z)$ becomes a step function $\Theta(z)$, so that the phase $\phi_E(z)$ incorporates only the external $E_{IR}(z, t)$ behavior. We also neglect any remaining z dependence of $\phi_E(z)$ since the variation of the net IR field on the vacuum side occurs on its wavelength scale (≈ 800 nm), which is much larger than the spatial extension of the SS.

Under these approximations, a z-independent Fresnel phase $\phi_E(z) \equiv \phi_E$ appears in the dipole element calculation.

As the envelope $h_{\mathrm{env}}(t_d)$ extends over more than a few IR cycles, the central frequency ω_{IR} is the dominant term in the right-hand side of Eq. (A8), meaning that absorptions or emissions of photon energies $\hbar\omega_{\mathrm{IR}}$ are the most likely. This allows us to approximate Eq. (A9) by retaining one factor of the product and two terms from the sum.

Defining the complex integral

$$I^{2n+1,(\pm)}_{k_{fz},i}(\omega_{\mathrm{IR}}) = \int dz\,dt\, e^{-i[k_{fz}+A_{\mathrm{IR},z}(\mathbf{r},t_d)]\cdot z} f_{\varepsilon_f,\theta_f}(z) z e^{i(2n+1)\omega_{\mathrm{IR}} t_d}$$
$$\times \psi_i(z) J_1\left(\frac{\mathbf{k}_f \cdot \hat{\mathbf{z}}}{\omega_{\mathrm{IR}}^2} \widetilde{E}(\omega_{\mathrm{IR}},z)\right) e^{\pm i\omega_{\mathrm{IR}} t_d}, \qquad (B1)$$

and rewriting it in complex polar representation,

$$I^{2n\pm1,(\pm)}_{k_{fz},i}(\omega_{\mathrm{IR}}) = \left| I^{2n\pm1,(\pm)}_{k_{fz},i}(\omega_{\mathrm{IR}}) \right| e^{i(\phi^{\pm}_{2n\pm1}+\phi^{\mathrm{HH}}_{2n+1})}, \qquad (B2)$$

we can express the transition matrix element (15) in complex polar representation for a final momentum $\mathbf{k}_f$ corresponding to SB2n,

$$T_{\mathbf{k}_f,\mathbf{k}_i}(\tau) \propto \delta_{\mathbf{k}_{f\parallel}\mathbf{k}_{i\parallel}}\Big[\big| I^{2n+1,(-)}_{k_{fz},i}(\omega_{\mathrm{IR}}) \big| e^{-i(-\omega_{\mathrm{IR}}\tau+\phi_E)+i(\phi^{-}_{2n+1}+\phi^{\mathrm{HH}}_{2n+1})}$$
$$+ \big| I^{2n-1,(+)}_{k_{fz},i}(\omega_{\mathrm{IR}}) \big| e^{i(-\omega_{\mathrm{IR}}\tau+\phi_E)+i(\phi^{+}_{2n-1}+\phi^{\mathrm{HH}}_{2n-1})} \Big]. \quad (B3)$$

The phases $\phi^{\pm}_{2n\pm1}$ are accumulated by the photoelectron due to one-photon XUV absorption and the absorption/release of a single IR photon.

The photoemission probability now becomes

$$P(\mathbf{k}_f,\tau) \propto P_0 + P_1 \cos\left(2\omega_{\mathrm{IR}}\tau - \phi^{\mathrm{RAB}}_{2n}\right), \qquad (B4)$$

with the raw RABBITT phase

$$\phi^{RAB}_{2n} \equiv \phi^{+}_{2n-1} - \phi^{-}_{2n+1} - \phi^{(\mathrm{HH})}_{2n-1} + \phi^{(\mathrm{HH})}_{2n+1} + 2\phi_E. \qquad (B5)$$

This definition of the RABBITT phase is similar to the one in Ref. [2], however, we explicitly expressed it in terms of the scattering phase difference $\phi^{+}_{2n-1} - \phi^{-}_{2n+1}$ and the Fresnel contribution $2\phi_E$. Numerically calculated raw RABBITT
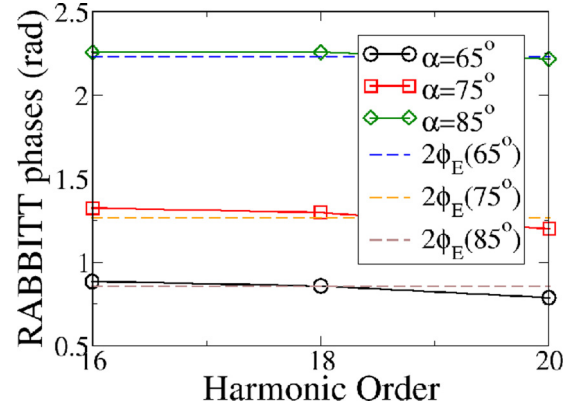
FIG. 15. Raw RABBITT phases for photoemission from the Cu(111) surface state for sideband orders 16–20 and incidence angles α of the APT and IR-laser pulse, compared with twice the Fresnel phase ϕ_E for each angle α.

phases for photoemission from the Cu(111) SS for three APT- and IR-incidence angles are shown in Fig. 15, displaying the $2\phi_E$ Fresnel contribution predicted analytically above. The RABBITT phases' close agreement with $2\phi_E$ for the three incidence angles and all SB orders indicates that RABBITT phases are essentially determined by the Fresnel phases, with only small contributions accumulated by dynamical interactions of the SS photoelectrons. This makes the SS a distinguished reference state for comparative RABBITT investigations.

The physical interpretation of the presence of the phase contribution $2\phi_E$ is that one of the two interfering two-photon processes involves the absorption of an IR photon, contributing a phase ϕ_E, while the other, an emission, contributes with the same phase increment albeit with reversed sign. Therefore, the two processes' relative phase is $2\phi_E$, which translates directly to the SS RABBITT phases, as shown analytically and numerically. We note that our numerical simulations presented in the main body of this manuscript and by the markers in Fig. 15 do not involve the assumptions made in this appendix (slowly varying IR-pulse envelope, no IR penetration, and the SS lying entirely outside of the material).

[1] S. Hüfner, *Photoelectron Spectroscopy. Principles and Applications* (Springer, Berlin, 2003).

[2] P. M. Paul, E. S. Toma, P. Breger, G. Mullot, F. Augé, P. Balcou, H. G. Muller, and P. Agostini, Science **292**, 1689 (2001).

[3] R. Kienberger, E. Goulielmakis, M. Uiberacker, A. Baltuska, V. Yakovlev, F. Bammer, A. Scrinzi, T. Westerwalbesloh, U. Kleineberg, U. Heinzmann, M. Drescher, and F. Krausz, Nature (London) **427**, 817 (2004).

[4] G. Sansone, E. Benedetti, F. Calegari, C. Vozzi, L. Avaldi, R. Flammini, L. Poletto, P. Villoresi, C. Altucci, R. Velotta, S. Stagira, S. De Silvestri, and M. Nisoli, Science **314**, 443 (2006).

[5] E. Goulielmakis, M. Schultze, M. Hofstetter, V. S. Yakovlev, J. Gagnon, M. Uiberacker, A. L. Aquila, E. M. Gullikson, D. T. Attwood, R. Kienberger, F. Krausz, and U. Kleineberg, Science **320**, 1614 (2008).

[6] M. Hentschel, R. Kienberger, C. Spielmann, G. A. Reider, N. Milosevic, T. Brabec, P. Corkum, U. Heinzmann, M. Drescher, and F. Krausz, Nature (London) **414**, 509 (2001).

[7] M. Schultze, M. Fieß, N. Karpowicz, J. Gagnon, M. Korbman, M. Hofstetter, S. Neppl, A. L. Cavalieri, Y. Komninos, T. Mercouris, C. A. Nicolaides, R. Pazourek, S. Nagele, J. Feist, J. Burgdörfer, A. M. Azzeer, R. Ernstorfer, R. Kienberger, U. Kleineberg, E. Goulielmakis, F. Krausz, and V. S. Yakovlev, Science **328**, 1658 (2010).

[8] S. Neppl, R. Ernstorfer, A. L. Cavalieri, C. Lemell, G. Wachter, E. Magerl, E. M. Bothschafter, M. Jobst, M. Hofstetter, U. Kleineberg, J. V. Barth, D. Menzel, J. Burgdörfer, P. Feulner, F. Krausz, and R. Kienberger, Nature (London) **517**, 342 (2015).

[9] V. Yakovlev, M. Korbman, and A. Scrinzi, Chem. Phys. **414**, 26 (2013).

[10] J. Mauritsson, M. B. Gaarde, and K. J. Schafer, Phys. Rev. A **72**, 013401 (2005).

[11] K. Klünder, J. M. Dahlström, M. Gisselbrecht, T. Fordell, M. Swoboda, D. Guénot, P. Johnsson, J. Caillat, J. Mauritsson, A. Maquet, R. Taïeb, and A. L'Huillier, Phys. Rev. Lett. **106**, 143002 (2011).

[12] R. Locher, L. Castiglioni, M. Lucchini, M. Greif, L. Gallmann, J. Osterwalder, M. Hengsberger, and U. Keller, Optica **2**, 405 (2015).

[13] M. Lucchini, A. Ludwig, L. Kasmi, L. Gallmann, and U. Keller, Opt. Express **23**, 8867 (2015).

[14] C. Palatchi, J. M. Dahlström, A. S. Kheifets, I. A. Ivanov, D. M. Canaday, P. Agostini, and L. F. DiMauro, J. Phys. B **47**, 245003 (2014).

[15] Z. Tao, C. Chen, T. Szilvási, M. Keller, M. Mavrikakis, H. Kapteyn, and M. Murnane, Science **353**, 62 (2016).

[16] D. Guénot, K. Klünder, C. L. Arnold, D. Kroon, J. M. Dahlström, M. Miranda, T. Fordell, M. Gisselbrecht, P. Johnsson, J. Mauritsson, E. Lindroth, A. Maquet, R. Taïeb, A. L'Huillier, and A. S. Kheifets, Phys. Rev. A **85**, 053424 (2012).

[17] A. S. Kheifets and I. A. Ivanov, Phys. Rev. Lett. **105**, 233002 (2010).

[18] A. L. Cavalieri, N. Muller, T. Uphues, V. S. Yakovlev, A. Baltuska, B. Horvath, B. Schmidt, L. Blumel, R. Holzwarth, S. Hendel, M. Drescher, U. Kleineberg, P. M. Echenique, R. Kienberger, F. Krausz, and U. Heinzmann, Nature (London) **449**, 1029 (2007).

[19] U. Thumm, Q. Liao, E. M. Bothschafter, F. Süßmann, M. F. Kling, and R. Kienberger, in *The Oxford Handbook of Innovation*, edited by D. Andrew (Wiley, New York, 2015), Chap. 13.

[20] C. Lemell, B. Solleder, K. Tőkési, and J. Burgdörfer, Phys. Rev. A **79**, 062901 (2009).

[21] Q. Liao and U. Thumm, Phys. Rev. A **89**, 033849 (2014).

[22] S. R. Leone, C. W. McCurdy, J. Burgdorfer, L. S. Cederbaum, Z. Chang, N. Dudovich, J. Feist, C. H. Greene, M. Ivanov, R. Kienberger, U. Keller, M. F. Kling, Z.-H. Loh, T. Pfeifer, A. N. Pfeiffer, R. Santra, K. Schafer, A. Stolow, U. Thumm, and M. J. J. Vrakking, Nat. Photon. **8**, 162 (2014).

[23] Q. Liao and U. Thumm, Phys. Rev. Lett. **112**, 023602 (2014).

[24] A. K. Kazansky and P. M. Echenique, Phys. Rev. B **81**, 193413 (2010).

[25] C.-H. Zhang and U. Thumm, Phys. Rev. A **84**, 065403 (2011).

[26] M. Lupetti, J. Hengster, T. Uphues, and A. Scrinzi, Phys. Rev. Lett. **113**, 113903 (2014).

[27] E. E. Krasovskii, V. M. Silkin, V. U. Nazarov, P. M. Echenique, and E. V. Chulkov, Phys. Rev. B **82**, 125102 (2010).

[28] L. Miaja-Avila, C. Lei, M. Aeschlimann, J. L. Gland, M. M. Murnane, H. C. Kapteyn, and G. Saathoff, Phys. Rev. Lett. **97**, 113604 (2006).

[29] G. Saathoff, L. Miaja-Avila, M. Aeschlimann, M. M. Murnane, and H. C. Kapteyn, Phys. Rev. A **77**, 022903 (2008).

[30] S. L. Hulbert, P. D. Johnson, M. Weinert, and R. F. Garrett, Phys. Rev. B **33**, 760 (1986).

[31] F. J. Himpsel and J. E. Ortega, Phys. Rev. B **46**, 9719 (1992).

[32] U. Höfer, I. L. Shumay, C. Reuß, U. Thomann, W. Wallauer, and T. Fauster, Science **277**, 1480 (1997).

[33] M. Wolf, E. Knoesel, and T. Hertel, Phys. Rev. B **54**, R5295 (1996).

[34] P. J. Jennings, R. O. Jones, and M. Weinert, Phys. Rev. B **37**, 6113 (1988).

[35] N. V. Smith, C. T. Chen, and M. Weinert, Phys. Rev. B **40**, 7565 (1989).

[36] E. Chulkov, V. Silkin, and P. Echenique, Surf. Sci. **437**, 330 (1999).

[37] H. Chakraborty, T. Niederhausen, and U. Thumm, Phys. Rev. A **70**, 052903 (2004).

[38] F. Roth, C. Lupulescu, E. Darlatt, A. Gottwald, and W. Eberhardt, J. Electron Spectrosc. **208**, 2 (2016).

[39] C. A. Rios Rubiano, M. S. Gravielle, D. M. Mitnik, and V. M. Silkin, Phys. Rev. A **85**, 043422 (2012).

[40] U. Thumm and J. Briggs, Nucl. Instrum. Methods Phys. Res., Sect. B **43**, 471 (1989).

[41] W. Greiner, *Classical Electromagnetism* (Springer, New York, 1996).

[42] N. W. Ashcroft and N. D. Mermin, *Solid State Physics* (Hardcourt College Publishers, Orlando, 1976).

[43] A. D. Rakić, A. B. Djurišić, J. M. Elazar, and M. L. Majewski, Appl. Opt. **37**, 5271 (1998).

[44] P. B. Johnson and R. W. Christy, Phys. Rev. B **6**, 4370 (1972).

[45] S. Tanuma, C. J. Powell, and D. R. Penn, Surf. Interface Anal. **43**, 689 (2011).

[46] V. Véniard, R. Taïeb, and A. Maquet, Phys. Rev. A **54**, 721 (1996).

[47] P. Antoine, A. L'Huillier, and M. Lewenstein, Phys. Rev. Lett. **77**, 1234 (1996).

[48] N. A. Papadogiannis, B. Witzel, C. Kalpouzos, and D. Charalambidis, Phys. Rev. Lett. **83**, 4289 (1999).

[49] C.-H. Zhang and U. Thumm, Phys. Rev. A **80**, 032902 (2009).

[50] D. W. Lynch and W. R. Hunter, in *The Oxford Handbook of Innovation*, edited by E. Palik (Academic Press, San Diego, 1998).

[51] J. B. W. Webber, Meas. Sci. Technol. **24**, 027001 (2013).

[52] J. D. Faires and R. L. Burden, *Numerical Methods* (Cengage Learning Inc., San Francisco, 2002), Chap. 4.